Journal of Luminescence 211 (2019) 100–107

Contents lists available at ScienceDirect

Journal of Luminescence

journal homepage: www.elsevier.com/locate/jlumin

Infrared spectroscopic properties of low-phonon lanthanide-doped $KLuS_2$ crystals

Jan Šulc[a,*], Richard Švejkar[a], Martin Fibrich[a], Helena Jelínková[a], Lubomír Havlák[b], Vítězslav Jarý[b], Martin Ledinský[b], Martin Nikl[b], Jan Bárta[a,b], Maksym Buryi[b], Roberto Lorenzi[c], Francesca Cova[c], Anna Vedda[c]

[a] Faculty of Nuclear Sciences and Physical Engineering, Czech Technical University in Prague, Břehová 7, Prague 1, 115 19, Czech Republic
[b] Institute of Physics of the Czech Academy of Sciences, Cukrovarnická 10, Prague 6, 162 00, Czech Republic
[c] Department of Materials Science, University of Milano - Bicocca, via Cozzi 55, 20125 Milano, Italy

ARTICLE INFO

Keywords:
Ternary sulfides
Low-phonon laser materials
Rare-earth doping
Infrared lasers
Golden ratio doping

ABSTRACT

$KLuS_2$ single crystal samples undoped and doped with a low (5 %) or high (38 %) concentration of trivalent thulium or ytterbium ions were synthesized in the form of thin hexagonal plates. The low phonon energy (~ 220 cm^{-1}) was confirmed using Raman spectroscopy. Samples were studied also by using optical absorption and emission as well as electron paramagnetic resonance spectroscopy and the observed spectral features are discussed. In particular, the 5 % Yb doped samples demonstrate homogeneous dopant distribution inside the material over the lutetium sites. No other signals either from potassium site or the exchange coupled ions were detected. For infrared transitions the luminescence kinetic was determined. Significantly broad infrared emission bands (at 1.4, 1.8 and 2.3 μm for Tm^{3+}, 1 μm for Yb^{3+}) and long decay times (e.g. 0.4 ms from $^3H_4$ to 19 ms from $^3F_4$ levels of Tm^{3+}, 1.4 ms from $^2F_{5/2}$ level of Yb^{3+}) make those materials perspective for future laser development.

1. Introduction

Rare-earth (RE) doped low-phonon matrices are important materials for construction of direct mid-infrared laser sources [1,2]. The phonon energy influences the overall infrared transparency range, which is important for laser operation, the rate of multiphonon relaxation of laser transitions, and also the phonon-assisted energy transfer processes, which can depopulate (or populate) laser levels [3–7].

The lowest phonon energies (E_{ph} ~ 140 – 200 cm^{-1}) in crystalline laser matrices have been reported for alkali-lead halides MPb_2X_5 (M = Rb, K; X = Cl, Br) [8–11]. Laser emission was successfully demonstrated with KPb_2Cl_5 doped by Pr^{3+}, Nd^{3+}, Dy^{3+}, or Er^{3+} ions [12–16]. Important and well-developed low-phonon laser host materials are also chalcogenide crystals (E_{ph} ~ 200 – 350 cm^{-1}), like Cr^{2+} and Fe^{2+} doped II-VI semiconductor compounds, [17–23] or thiogallates $CaGa_2S_4$ or $PbGa_2S_4$, for which the laser action was obtained under Dy^{3+} doping [12,24–26]. Great advantage of all these materials is low or zero hygroscopicity, but they usually suffer from low RE-dopant acceptance, which limits the doping concentration to several percent or less [10].

The family of ternary alkali RE sulfides with general formula $ALnS_2$ (A = K, Rb; Ln = RE elements, usually La, Gd, Lu, or Y) belongs among the new promising low-phonon chalcogenide materials [27–29]. The trivalent lanthanide cation site in $ALnS_2$ structure has a suitable size to accommodate RE^{3+} ions, which allows a very high homogenous RE-doping without segregation or charge compensation problems [29]. About 40 % larger distance between trivalent Ln-Ln cations in comparison with Ga-Ga distance in thiogallates also allows higher RE^{3+} doping levels before concentration quenching occurs [27,30]. This new family of RE-doped ternary sulfides shows prospective applications for X-ray and white LED phosphors and their spectroscopy in UV and VIS spectral range was studied in detail [27–29,31–33]. It was also confirmed that $KLuS_2$ is a moisture-resistant, long-term and high-temperature stable material.

All ternary sulfides $ALnS_2$ with A = K or Rb adopt the α-$NaFeO_2$-type rhombohedral structure (space group R$\bar{3}$m) with alternating layers

* Corresponding author.
E-mail addresses: jan.sulc@fjfi.cvut.cz (J. Šulc), Richard.Svejkar@fjfi.cvut.cz (R. Švejkar), martin.fibrich@fjfi.cvut.cz (M. Fibrich), helena.jelinkova@fjfi.cvut.cz (H. Jelínková), havlak@fzu.cz (L. Havlák), jary@fzu.cz (V. Jarý), ledinsky@fzu.cz (M. Ledinský), nikl@fzu.cz (M. Nikl), bartaj@fzu.cz (J. Bárta), buryi@fzu.cz (M. Buryi), roberto.lorenzi@unimib.it (R. Lorenzi), francesca.cova@unimib.it (F. Cova), anna.vedda@unimib.it (A. Vedda).

https://doi.org/10.1016/j.jlumin.2019.03.005
Received 10 January 2019; Received in revised form 1 March 2019; Accepted 3 March 2019
Available online 07 March 2019

composed of edge-sharing AS_6 and LnS_6 octahedra. Generally, the structure is described in hexagonal setting as A^+ ions occupying the 3a Wyckoff sites (0 0 0), the Ln^{3+} ions residing at the 3b sites (0 0 1/2), while sulfur anions can be found at the 6c (0 0 *z*) sites [30,34]. The sulfur coordinate *z* determines the trigonal distortion of the AS_6 and LnS_6 octahedra, which are slightly elongated or shortened along the ***c*** axis, respectively, to better accommodate the larger alkali metals (K, Rb) and the smaller rare-earth elements. Thus, the ideal O_h symmetry reduces to a D_{3d} local symmetry in both types of octahedra. Recently, new structural determinations of $ALnS_2$ [30,34,35] were published that indicate a systematic error in former structure determinations. The fractional *z* (S^{2-}) coordinate in alkali RE sulfides is a good parameter for simple monitoring of structural trends (see Fig. 6 in Ref. [30], Fig. 2 in Ref. [35] and Fig. 9 in Ref. [34]). However, the lattice parameters are also extremely important structural parameters, with *a* being closely associated mainly with the size of rare-earth ions ($a \sim 3.8 - 4.3$ Å) and *c* corresponding to the size of A^+ ($c \sim 21.7 - 21.9$ Å for K, $22.7 - 22.9$ Å for Rb) [30]. For Pr-doped $RbGdS_2$ a linear increase in lattice parameter *a* was observed [36] in accordance with the Vegard's rule, indicating the presence of true solid solution and suitability of the host for incorporation of large amounts of lanthanide dopants.

In this paper, we focused on the study of Yb and Tm-doped $KLuS_2$ ternary sulfides from the future infrared laser development point of view.

2. Material and methods

2.1. Sample preparation

The pure $KLuS_2$ or doped $KLu_{0.95}Tm_{0.05}S_2$, $KLu_{0.62}Tm_{0.38}S_2$, $KLu_{0.9995}Yb_{0.0005}S_2$, $KLu_{0.95}Yb_{0.05}S_2$, $KLu_{0.62}Yb_{0.38}S_2$ crystalline samples were synthesized according to the scheme given by Ref. [27]. The starting materials were 4N7 K_2CO_3, 5N Lu_2O_3, 3N Tm_2O_3 (for $KLu_{0.95}Tm_{0.05}S_2$), 4N7 Tm_2O_3 (for $KLu_{0.62}Tm_{0.38}S_2$) and 4N Yb_2O_3 for $KLu_{0.9995}Yb_{0.0005}S_2$, $KLu_{0.95}Yb_{0.05}S_2$ and $KLu_{0.62}Yb_{0.38}S_2$. The gases used during the synthesis were 5N Ar and 2N5 H_2S. The chemical reactions were carried out in a corundum tube (2N7 Al_2O_3). The tube was placed in an electric resistance furnace equipped with heating/cooling-rate regulation. Either Ar or H_2S gas was allowed to flow into the reaction tube. The gases were taken directly from pressurized cylinders using a three-way stopcock to switch between them. A mixture of the K_2CO_3 with Tm_2O_3- or Yb_2O_3-doped Lu_2O_3 in the molar ratio 80: 1 was used as the starting material. Tm or Yb doping was carried out by the simple mixing and grinding of Lu_2O_3 and Tm_2O_3 or Yb_2O_3. For example, for the preparation of $KLu_{0.62}Tm_{0.38}S_2$ 0.080 mol (= 11.0564 g) K_2CO_3, 0.000618 mol (= 0.2459 g) Lu_2O_3 and 0.000382 mol (= 0.1474 g) Tm_2O_3 was used. The molar quantities of Lu_2O_3 and Tm_2O_3 (or Yb_2O_3) were in the golden ratio in $KLu_{0.62}Tm_{0.38}S_2$ or $KLu_{0.62}Yb_{0.38}S_2$.

Prior to the reaction itself, the reagents (K_2CO_3 and Lu_2O_3:Tm_2O_3 or Lu_2O_3:Yb_2O_3) were homogenized in an agate mortar. The mixture was placed in a corundum boat (2N7 Al_2O_3) and inserted into the corundum tube (inner volume about 1 dm^3). The mixture was then heated to 1323 K using the electric resistance furnace (heating rate 10 K/min) under a flow of Ar (30 dm^3/h). After the desired temperature had been reached, the reaction mixture was annealed for 2 h under a flow of H_2S (15 dm^3/h). Following annealing, the system was cooled under a flow of Ar (0.5 K/min, 0.3 dm^3/h). Upon reaching room temperature, the corundum boat was removed from the tube furnace and the reaction products were purified by suspension and decantation, three times with distilled water and once with acetone. K_2S was removed by water, while pure or doped $KLuS_2$ samples were left behind. The resulting products consisted of ~ 40 μm thick platelets with imperfect hexagonal morphology sized up to 3 × 4 mm. Photograph of the $KLu_{0.95}Tm_{0.05}S_2$ is presented in Fig. 1.

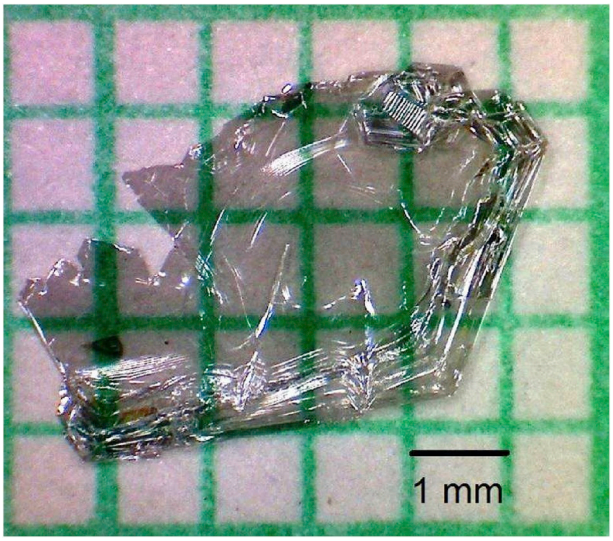

Fig. 1. A photograph of the $KLu_{0.95}Tm_{0.05}S_2$.

2.2. Methods of characterization

The structural characterization and phase purity assessment was performed by X-ray powder diffraction (XRD) using Rigaku MiniFlex 600 diffractometer equipped with Ni-filtered Cu X-ray tube and NaI:Tl scintillation detector. The diffraction patterns were recorded between 10° and 80° 2θ on pure or powdered samples, which were deposited onto glass holders. The diffraction patterns were then compared with the relevant ICDD PDF-2 database records and the lattice parameters were calculated from diffraction peak positions. EPR spectra were measured in the X-band (9.4 GHz) on a commercial Bruker X/Q-band E580 FT/CW ELEXSYS spectrometer at the 25 K in an Oxford Instruments ESR900 continuous flow cryostat. All simulations have been done in the *Easyspin toolbox 5.1.12* program [37]. Raman spectra were measured by InVia Reflex micro-spectrometer from Renishaw with 442 nm He-Cd excitation laser and collected for 60 s by 50× objective. The laser mean power was 30 mW in order to eliminate sample heating. The absorption spectra of the samples were measured in the range from 200 to 2050 nm using a Shimadzu UV-3600 spectrophotometer (sampling interval 0.5 nm and resolution 5 nm). The fluorescence was excited by a pulsed laser diode emitting at λ_{ex} = 793 nm in the case of Tm-doped samples or 970 nm for Yb-doped samples (excitation pulse width 2 ms, repetition rate 10 Hz). The emission spectra of Tm-doped $KLuS_2$ in the vicinity of 800 nm were measured by fiber spectrometer StellarNet BlueWave NIR 50 (Si detector, sampling interval 0.5 nm). The same spectrometer in combination with fiber spectrometer Ocean Optics NIR 512 (InGaAs detector, sampling interval 1.75 nm) was used to record the emission of Yb-doped $KLuS_2$ samples in spectral region 900–1500 nm. Due to a strong decrease of Si-detector sensitivity, its response was calibrated in respect to the InGaAs detector using tungsten lamp and the data from both detectors were joined at 1025 nm. To separate the overlapping excitation and emission spectra, the BlueWave NIR 50 spectrometer acquisition was triggered 0.5 ms after the end of excitation pulse. The emission spectra of Tm-doped $KLuS_2$ in near infrared region from 1100 up to 2500 nm were measured by stepper-motor driven Oriel monochromator 77250 (grating no. 77301, sampling 2 nm, resolution 10 nm) with the PbS detector (PDA30G, Thorlabs). GaAs or Ge filters were used to suppress the rest of excitation radiation and to eliminate the higher diffraction orders. The fluorescence intensity decay measurement around the wavelength of 1 μm was performed using the Si-PIN photodiode (HP 5082-4220, Hewlett Packard) and long-pass filter (FEL1000, Thorlabs). The time development of fluorescence decay for radiation wavelength in the range from 1200 to 1600 nm was observed by an InGaAs photodiode

(FGA10, Thorlabs). To separate the desired spectral range, the above mentioned monochromator was used in combination with appropriate long-pass or band-pass filter. The fluorescence intensity decay measurement around wavelength 1.8 μm was performed using a GaInAsSb-PIN photoreceptor (model PD36-05-TEC, IBSG Co.) together with Ge and band-pass filter (FB1750-500, Thorlabs). The photodiode signal was recorded and digitalized via oscilloscope (TDS 3052B, 500 MHz, 5 GS/s, Tektronix). For all measurements, the response time was better than 20 μs. All Raman, absorption and emission spectra together with fluorescence decay were measured at temperature $T = 300$ K.

3. Results and discussion

3.1. Composition of $KLuS_2$

The doped $KLuS_2$ samples were obtained in the form of transparent thin platelets with similar morphology as in pure $KLuS_2$ [31]; therefore, mainly the highly-doped samples (38 % Yb or Tm) were analyzed by XRD to determine phase purity of the material. Diffraction patterns of pristine platelets, oriented parallel to the surface of the glass sample holder, presents only the (0 0 n) lines consistent with $KLnS_2$. No other diffraction lines of $KLnS_2$ were observed, indicating perfect orientation of the crystals in the platelets, their normal vector coinciding with the ***c*** axis. After powdering of the samples in a ceramic mortar, strong preferred orientation in ⟨001⟩ direction remained, but weak diffraction lines corresponding to other directions of rhombohedral $KLnS_2$ appeared as well. No other diffraction lines or peak splitting were detected, confirming that the crystals were a single pure phase. Based on the diffraction lines positions, lattice parameters $a = 3.953(4)$ Å, $c = 21.862(3)$ Å and $a = 3.965(6)$ Å, $c = 21.865(6)$ Å were determined for $KLu_{0.62}Yb_{0.38}S_2$ and $KLu_{0.62}Tm_{0.38}S_2$, respectively. The lattice parameter c is fully consistent with K-based $ALnS_2$ ternary sulfides, whereas a is somewhat increased compared to that of pure $KLuS_2$ ($a = 3.9490(4)$ Å, $c = 21.871(3)$ Å [30]) due to the incorporation of slightly larger Yb^{3+} or Tm^{3+} ions, respectively. Based on the reported lattice parameters of $KYbS_2$ ($a = 3.9615(2)$ Å, $c = 21.810(3)$ Å [34]) and $KTmS_2$ ($a = 3.9761(5)$ Å, $c = 21.841(3)$ Å [34]) and the assumption of Vegard's rule, the values of a for the $KLu_{0.62}Yb_{0.38}S_2$ and $KLu_{0.62}Tm_{0.38}S_2$ samples should be approximately 3.954 Å and 3.959 Å, respectively. The measured values are within statistical uncertainty (imposed by the weak intensity of non-***c***-oriented peaks), indicating that the lanthanide ions are present in the crystals as a solid solution. However, the statistical uncertainties are large compared to the rather small difference between terminal compounds of the solid solution. Longer or more thorough grinding may improve the statistics, but at the risk of structural changes or increased microstructural strain.

3.2. EPR spectroscopy of $KLuS_2$:Yb

To have an insight into the local structure, energy levels and paramagnetic properties of the Yb^{3+} (4 f^{13} outer shell) inside the $KLuS_2$ host electron paramagnetic resonance measurements were carried out. The EPR spectrum measured at the **B**⊥**c** external magnetic field orientation is shown in Fig. 2 (I).

The spectrum has been fitted by the calculated one using the following spin-Hamiltonian:

$$\hat{H} = g\beta_e \tilde{S}_z B + A(^{171}\mathrm{Yb})\tilde{S}_z \tilde{I}_z(^{171}\mathrm{Yb}) + A(^{173}\mathrm{Yb})\tilde{S}_z \tilde{I}_z(^{173}\mathrm{Yb}) \quad (1)$$

where g, β_e, B are the g factor, Bohr magneton, and magnetic field, respectively; $A(^{171,173}\mathrm{Yb})$ are the ^{171}Yb (nuclear spin $I = 1/2$, abundance ~ 14 %) and ^{173}Yb (nuclear spin $I = 5/2$, abundance ~ 16 %) hyperfine (HF) constants; $\tilde{S}_z$, $\tilde{I}_z$ are the effective electron and nuclear z-component spin operator. The $g = 3.2333$ and $A(^{171}\mathrm{Yb}) = 2666.4$ MHz, $A(^{173}\mathrm{Yb}) = 700$ MHz.

Experimental angular dependence of the spectrum center of gravity resonance magnetic field was plotted in Fig. 2(II) in the **B**⊥**c** → **B**||**c** rotational plane along with the calculated fitting curve. For the fitting the first term in spin-Hamiltonian in Eq. (1) was used. The **g** tensor main values as well as the principal axes frame orientation represented by Euler angles were determined: $g_\perp = 3.2333 \pm 0.0003$ and $g_\parallel = 0.27 \pm 0.05$, $\alpha = \beta = 0°$, $\beta = -6$ °. The − 6 ° deviation from 0 ° in the β angle is most probably due to very small sample dimensions and inhomogeneous sample thickness (flake shape). This has caused slight **c** axis deviation from the external magnetic field direction due to the creation of stable tensions inside the sample bulk. Along with this the large error in the $g_\parallel$ value determination is due to very steep angular dependence when approaching the **c** axis during the sample rotation. In the (0001) rotational plane the spectrum exhibits almost isotropic feature and thus it has not been taken into consideration.

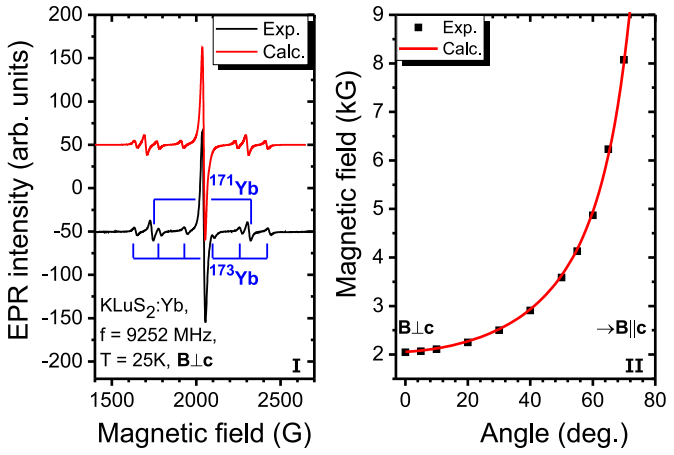

Fig. 2. I – EPR spectra, the experimental and the calculated one, with the hyperfine structures from the ^{171,173}Yb indicated by grates. II – experimental angular dependence (dots) of the Yb^{3+} resonances in the **B**⊥**c** → **B**||**c** rotational plane fitted by the calculated one.

Since only one EPR spectrum was measured (Fig. 2(I)) and Yb^{3+} and Lu^{3+} crystal radii are very similar, 1.008 Å and 1.001 Å [38], respectively, the Yb^{3+} ions were supposed to occupy only lutetium sites in the $KLuS_2$ host. No signs of the doublets of resonance lines which might originate from the Yb^{3+}–Yb^{3+} exchange coupling (dimers) were observed in the EPR spectra unless these coupled ions are too far from one another so the interaction between them is of the order of the resonance linewidth (~ 20 G, Fig. 2(I)). The 20 G linewidth is, most probably, the result of dipolar broadening [39,40]. This corroborates homogeneous distribution of the ytterbium ions inside the material without clustering.

The lowest Yb^{3+} energy level due to spin orbit coupling is $^2F_{7/2}$ [39,40]. The local crystal field of trigonal symmetry, for example, in Ref. [41] it was supposed to be D_{3d} for the Eu^{2+}, will split it into four Kramers doublets $|J, M_J\rangle$: $|7/2, \pm 7/2\rangle$, $|7/2, \pm 5/2\rangle$, $|7/2, \pm 3/2\rangle$ and $|7/2, \pm 1/2\rangle$. Calculations done similarly to that reported for Ce^{3+} [39,40] show that the doublet results in $g_\perp = 4.57$ and $g_\parallel = 1.14$. Other doublets are responsible for much higher g factors. Therefore, one may conclude comparing these values with the ones obtained experimentally that the lowest state is namely the $|7/2, \pm 1/2\rangle$, however, with admixture of some other levels. Assuming the relatively high local crystal field D_{3d} symmetry the experimental $g_\perp = 3.2333$ and $g_\parallel = 0.27$ values in the first order of the crystal field theory or even in the second could not be reached. This leads to conclusion that the symmetry is lower allowing mixing of the states which differ in M_J by 3 [39]. The symmetry should allow high order terms to a Hamiltonian. It can be C_{3v} a subgroup of the D_{3d} [42]. By trying simple calculations in the first order with the lowest doublet composed under this requirement: $\cos\theta|7/2, \pm 1/2\rangle \pm \sin\theta|7/2, \mp 5/2\rangle$ [39] it was impossible to find θ satisfying experimental g factor values, however, if the $g_\perp = 3.2333$ held on, the lowest $g_\parallel = 0.73$ could be reached with $\theta \sim 14$ °, which is still

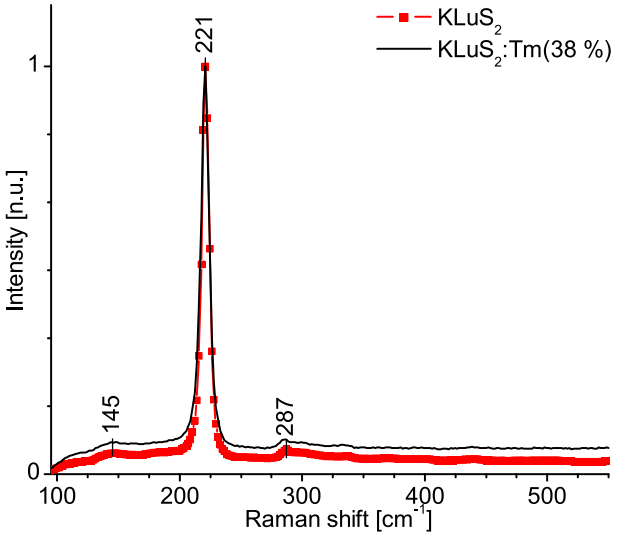

Fig. 3. The Raman spectra of pure $KLuS_2$ and $KLu_{0.62}Tm_{0.38}S_2$ samples.

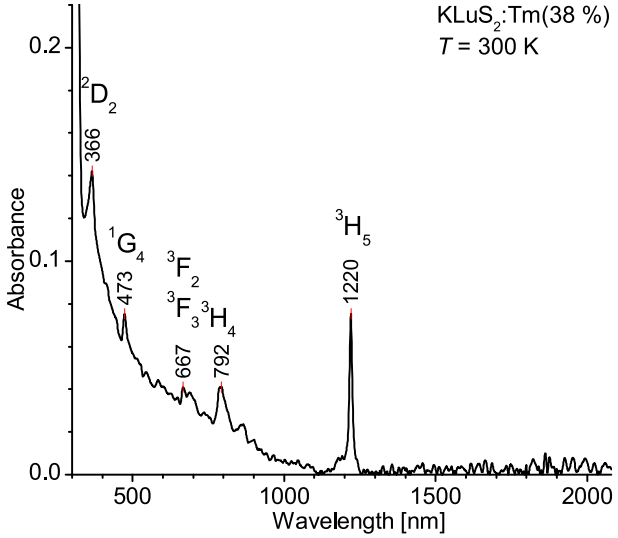

Fig. 4. The absorption spectra of $KLu_{0.62}Tm_{0.38}S_2$ sample.

almost three times larger than the $g_{||} = 0.27$ experimental value. Therefore, in the second order, the mixing of the triply split excited $^2F_{5/2}$ state to the ground $\cos\theta|7/2, \pm1/2\rangle \pm \sin\theta|7/2, \mp5/2\rangle$ is expected. This is well described for the Ce^{3+} in double lanthanide nitrates [43]. Our experimental data do not allow to carry out quantitative analysis of this problem.

3.3. Raman spectroscopy of $KLuS_2$

Pure $KLuS_2$ and $KLu_{0.62}Tm_{0.38}S_2$ samples were characterized by Raman spectroscopy; resulting spectra are depicted in Fig. 3 in the energy range of 95–550 cm^{-1}. From the results it follows that the substitution of a significant part of lutetium ions by thulium ions with similar mass had no significant influence on Raman spectrum and both samples give similar spectral features: a strong band at 221 cm^{-1} and weak bands peaking around 145 and 287 cm^{-1}. The vibrational origin of the measured bands has been discussed in literature [44]. The most prominent band at 221 cm^{-1} (10 cm^{-1} FWHM) and the second one peaking at 287 cm^{-1} could be assigned to the Raman active modes E_g and A_{1g} of point group D_{3d}, respectively.

As it was shown by Rademaker [9], the highest observed energy peak position can be a first approximation for effective phonon energy E_{ph} of host crystalline matrices. For $KLuS_2$ it was estimated to be $E_{ph} \sim 220$ cm^{-1}, which is comparable to other low-phonon materials like ZnSe ($E_{ph} \sim 250$ cm^{-1}) or KPb_2Cl_5 ($E_{ph} \sim 200$ cm^{-1}). This reduces the multiphonon interactions and should minimize the non-radiative decay, which could permit efficient radiative transitions at new wavelengths – both in mid-infrared and visible region.

3.4. Absorption spectra of Tm- and Yb-doped $KLuS_2$ samples

The measured absorption spectra of $KLu_{0.62}Tm_{0.38}S_2$ and $KLu_{0.62}Yb_{0.38}S_2$ samples are plotted in Fig. 4 and in Fig. 5, respectively. The form of investigated samples, especially the small thickness (~ 40 μm), caused that the absorption modulation was low and measured spectra were noisy even for highly doped samples. At the same time, for both Tm^{3+} and Yb^{3+} ions, the low strength of forbidden 4f-4f transition makes the measurements even more complicated. In spite of that, the presence of Tm^{3+} and Yb^{3+} ions in both samples is well manifested by their characteristic absorption lines. The non-zero background in visible part of absorption spectra could be explained by an uncorrected Fresnel losses or scattering on the samples. The strong and sharp absorption of Tm^{3+} at 1220 nm in $KLuS_2$ is remarkable, which is probably caused by the Tm^{3+} ion $^3H_6 \rightarrow {}^3H_5$ magnetic dipole transitions forced by the

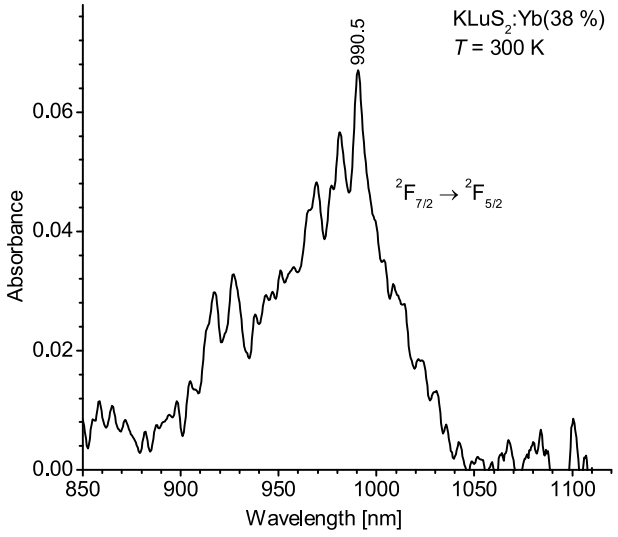

Fig. 5. The absorption spectra of $KLu_{0.62}Yb_{0.38}S_2$ sample.

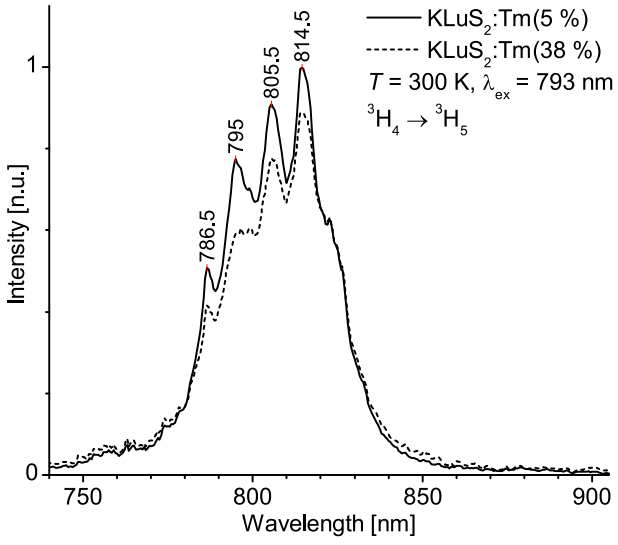

Fig. 6. The fluorescence spectra of Tm-doped $KLuS_2$ samples.

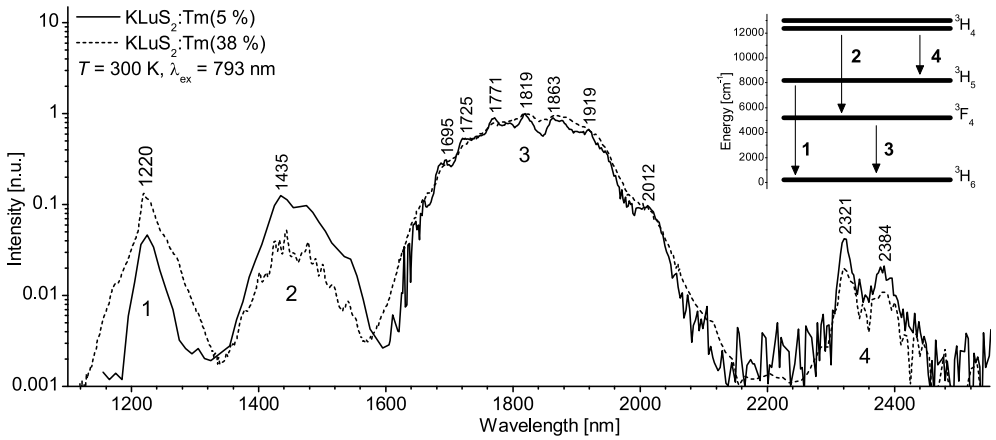

Fig. 7. The fluorescence spectra of Tm-doped $KLuS_2$ samples. The inset, containing the energy level diagram of Tm^{3+}, serve to denominate the observed emission bands.

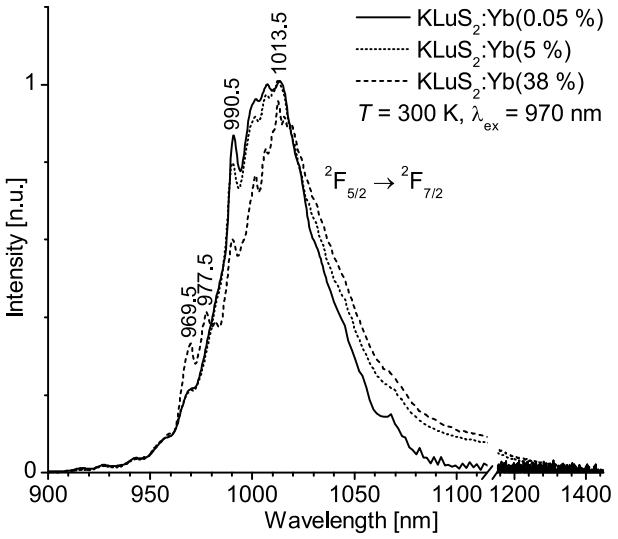

Fig. 8. The fluorescence spectra of Yb-doped $KLuS_2$ samples.

crystal field. This line is about one magnitude stronger than other lines, which could be interesting for applications in which interaction with the magnetic component of light takes place [45]. On the contrary, the mid-infrared absorption line corresponding to the $^3H_6 \rightarrow {}^3F_4$ transition of the Tm^{3+} ion was not observed in the absorption spectrum probably due to its low intensity. Because the corresponding emission was detected well, as will be discussed later, this transition is probably very broad and absorption modulation was lost in the noise. The absorption corresponding to the $^2F_{7/2} \rightarrow {}^2F_{5/2}$ transition of Yb^{3+} ion ranging from 900 up to 1040 nm is also exceptionally broad (see Fig. 5).

3.5. Fluorescence spectra of Tm- and Yb-doped $KLuS_2$ samples

The fluorescence spectra of tested Tm- and Yb-doped $KLuS_2$ samples with low and high doping were recorded at the broadest available range; the results are shown in Figs. 6–8.

In the case of Tm-doped $KLuS_2$, the $^3H_4$ manifold was excited and five emission lines having a maxima around 0.81, 1.22, 1.45, 1.82, and 2.32 μm were recorded and identified (see Figs. 6 and 7). The spectra for $^3H_4 \rightarrow {}^3H_5$ transition corresponding to ~ 800 nm emission are shown for both Tm-doping concentrations in Fig. 6. In both cases the spectrum is ~ 40 nm wide (FWHM) with four well resolved peaks. The small depletion of 795 nm peak in case of highly doped $KLuS_2$:Tm could be caused by fluorescence reabsorption, thus more precisely specifying the corresponding absorption peak position (see Fig. 4). Spectra for the other four fluorescence lines are shown in Fig. 7. There is also no significant difference between both samples varying in the Tm-doping. The first fluorescence line with maximum at 1220 nm corresponds to the $^3H_5 \rightarrow {}^3H_6$ transition. This line is remarkably intense confirming the low phonon energy of $KLuS_2$ – for materials with higher phonon energy the population of the $^3H_4$ level is depleted due to a non-radiative transition to the $^3F_5$ level and 1.2 μm line in fluorescence spectrum is not present. The next emission band, peaking at 1435 nm, corresponds to the $^3H_4 \rightarrow {}^3F_4$ transition. The line in the vicinity of 2.3 μm originates from the same level and corresponds to the $^3H_4 \rightarrow {}^3H_5$ transition. Both these transitions, together with above mentioned $^3H_4 \rightarrow {}^3H_5$ transition, are available for laser action and their presence in the emission spectrum proves that processes depopulating the $^3H_4$ level, like cross-relaxation, are limited in $KLuS_2$:Tm even for very high Tm-doping concentration. The probability of such processes could be reduced for two reasons: the low phonon energy in $KLuS_2$ may not be high enough to compensate for the energy difference between the $^3H_4 \rightarrow {}^3F_4$ and $^3H_6 \rightarrow {}^3F_4$ transitions; cross-relaxation is strongly sensitive to the donor-acceptor separation and the shortest possible distance between adjacent Tm-positions is relatively high [27,30]. It should be noted that radiative transition from the $^3H_5$ to the $^3F_4$ level, which should correspond to emission around 3.7 μm, was not detected. The strongest line (~ 220 nm FWHM), peaking at 1.82 μm, corresponds to the $^3F_4 \rightarrow {}^3H_6$ transition, which is commonly used for Tm-laser emission at 2 μm spectral region. The smooth and slowly decreasing long-wavelength tail of this line is promising for broad-band tuning and short pulse laser generation.

Due to the simple structure of Yb^{3+} ion levels, the fluorescence spectra of $KLuS_2$:Yb contain only one line corresponding to the $^2F_{5/2} \rightarrow {}^2F_{7/2}$ transition – see Fig. 8. This fluorescence band, having a maximum at 1013 nm, looks very compact and the observed differences between samples doped by 0.05, 5, and 38 % Yb is probably caused mainly by fluorescence reabsorption. For samples containing 5 and 38 % of Yb, this emission line has an exceptionably long and smooth tail lasting up to 1.2 μm; if the lasing will be reached, broad-band tuneability and short pulse generation could be expected.

3.6. Fluorescence decay of Tm- and Yb-doped $KLuS_2$ samples

The fluorescence decay curves related to the observed Tm^{3+} and Yb^{3+} ions transitions were recorded and are shown in Figs. 9–11 for Tm-doped $KLuS_2$, and in Fig. 12 for Yb-doped $KLuS_2$ samples, respectively. To estimate the corresponding fluorescence decay time(s) τ_1 (τ_2), double-exponential model $(I(t) = A\exp(-t/\tau_1) + (1 - A)\exp(-t/\tau_2))$ was used to fit the recorded fluorescence decay curve $I(t)$. The obtained

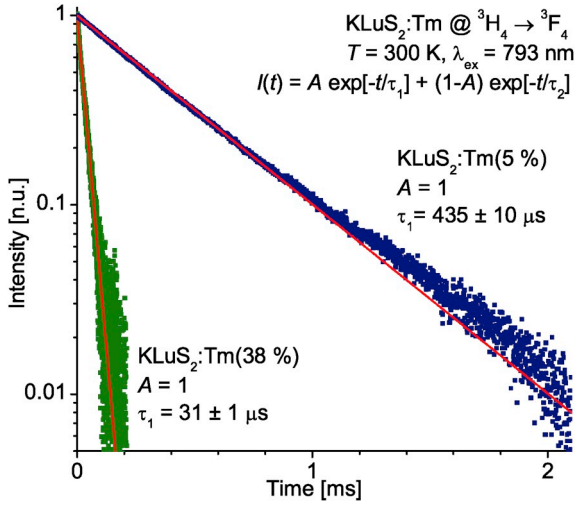

Fig. 9. The fluorescence decay curve of Tm-doped $KLuS_2$ samples – $^3H_4$ level.

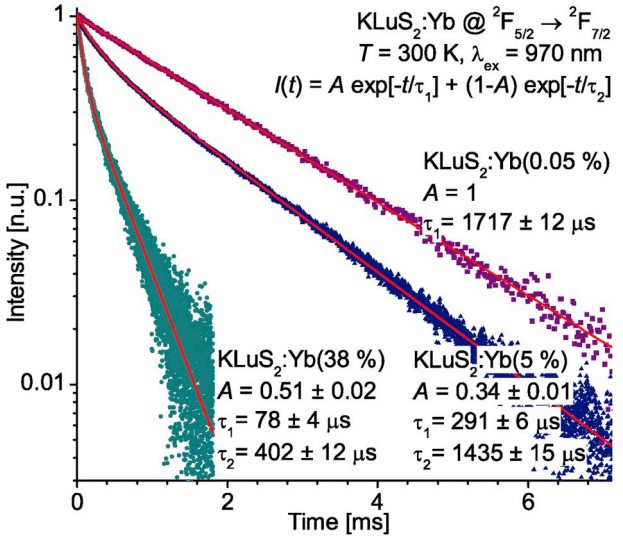

Fig. 12. The fluorescence decay curve of Yb-doped $KLuS_2$ samples.

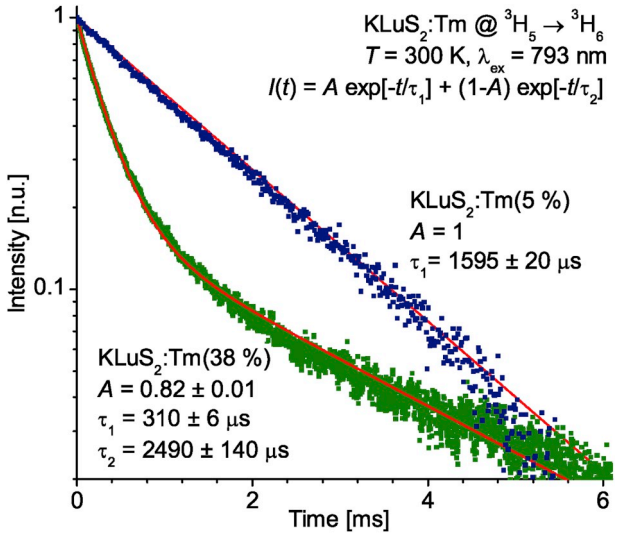

Fig. 10. The fluorescence decay curve of Tm-doped $KLuS_2$ samples – $^3H_5$ level.

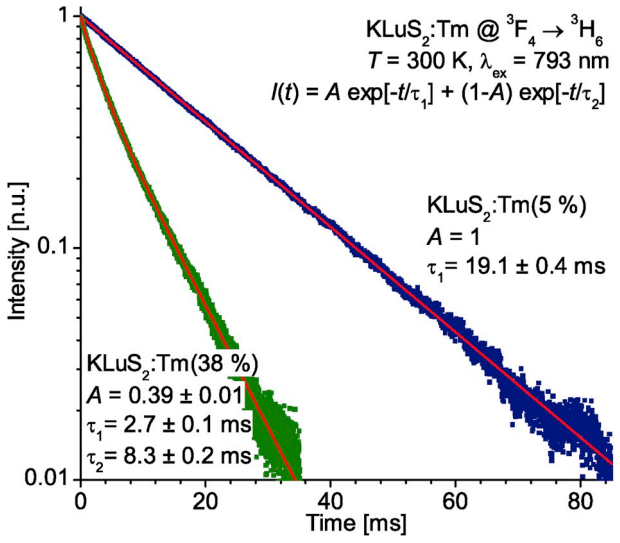

Fig. 11. The fluorescence decay curve of Tm-doped $KLuS_2$ samples – $^3F_4$ level.

results are presented together with the specific decay curve.

In the case of $KLuS_2$:Tm (5 %), the fluorescence decay was well modelled as a single-exponential with well-defined fluorescence decay time. The exceptionally long decay time for fluorescence starting from the $^3H_4$ level (~ 430 μs) suggests that the effect of phonon-assisted cross-relaxation process ($^3H_4 \rightarrow {}^3F_4$, $^3H_6 \rightarrow {}^3F_4$) is negligible for this Tm-doping level [6]. This fact could be interesting for future 2.3 μm laser construction. The lifetime of the potential 2 μm upper laser level ($^3F_4$) is also remarkably long, reaching 19 ms. The relatively long decay time 1.6 ms of unquenched 1.22 μm emission originating from the $^3H_5$ level is also worth mentioning. Stronger influence of some kind of ion-ion interaction resulting in fluorescence quenching and double-exponential decay was observed for the highly Tm-doped $KLuS_2$ sample only. Here, the mentioned cross-relaxation process depopulating the $^3H_4$ level is probably much stronger and the measured decay time is close to 30 μs. The decay time for the $^3F_4$ level was strongly quenched as well, but the fast decay component was still reasonably long (2.7 ms). Because the slow component of the $^3H_5$ level decay has a similar value (~ 2.5 ms), one can consider that there is some coupling between the $^3H_5$ and $^3F_4$ levels or that some new optical center was formed in the highly doped $KLuS_2$:Tm, but in fact the origin of double-exponential decay is not clear.

In the case of the $KLuS_2$:Yb, only the fluorescence from the very-low doped sample (0.05 % of Yb) had a single-exponential character with the decay time 1.72 ms. For both higher doped $KLuS_2$:Yb samples, the observed fluorescence decay curves had double-exponential character and concentration quenching is evident (see Fig. 12). In the case of low doping (5 % of Yb), the fast component (τ_1 = 0.29 ms) represented ~ 1/3 of the fluorescence signal and the stronger slow component has a reasonably long decay time (τ_2 = 1.44 ms). In the case of highly Yb-doped $KLuS_2$ (38 % of Yb), the concentration quenching had even stronger influence on the fluorescence decay and the decay times dropped significantly (τ_1 = 0.08 ms, τ_2 = 0.40 ms).

4. Conclusions

In this study, we present $KLuS_2$ single crystal as a new promising low-phonon, non-hygroscopic laser host for high-concentration lanthanide doping. In our case, Tm^{3+}- and Yb^{3+}-ion doped $KLuS_2$ samples were investigated. The transparent hexagonal-shaped platelets were shown to be pure rhombohedral phase consistent with $KLuS_2$ even in highly-doped samples, with small increase in lattice parameter *a* due to a larger size of dopants compared to Lu^{3+}. Based on the EPR data one may infer that the Yb^{3+} ions distribution inside the material ($KLuS_2$:Yb

(5 %)) is homogeneous since no signals which might come from coupled Yb^{3+}–Yb^{3+} ions (dimers) were observed in EPR spectra unless they are masked by the single ion spectrum. The ions are not creating clusters. As long as only one sort of signal from the Yb^{3+} was observed and comparing ionic radii of the Yb^{3+} and Lu^{3+} in the same octahedral coordination, the activator was assumed to occupy the Lu^{3+} sites, exclusively. Using Raman spectroscopy we found that the $KLuS_2$ phonon energy $E_{ph} \sim 220\ cm^{-1}$. We tested this material under low and high Tm- and Yb-doping. Even though the used preparation method allowed to synthesize the crystals only in the form of ~ 40 μm thick hexagonal plates with ~ 2 mm cross-section, the absorption was high enough to be measured using standard spectrophotometer, which allows us to identified positions of suitable excitation bands. Using laser diode, we were able to excite infrared emission. For particular transitions the corresponding emission spectra and luminescence decay time were measured. An exceptionally broad emission line of the $KLuS_2$:Yb was observed, spanning the wavelength range from 0.95 μm to 1.20 μm with the decay time ~ 1.4 ms for the reasonable level of doping (5 % of Yb). In the case of the $KLuS_2$:Tm samples, five infrared emission lines with the maxima around 0.81, 1.22, 1.45, 1.82, and 2.32 μm were detected. The emission lines at 0.81, 1.43 and 2.4 μm originating from the $^3H_4$ level of the Tm^{3+} ion, usually quenched in well-established Tm-doped materials, were remarkably strong. In the case of the $KLuS_2$:Tm (5 %) a single-exponential decay curve with the time constant ~ 430 μs was recorded, which proves that Tm-Tm cross-relaxation process depopulating the $^3H_4$ level is significantly reduced in low-doped $KLuS_2$:Tm and transitions starting from this level could be available for lasing. We can conclude that if future crystal growth process allows to obtain larger and thicker crystals, $KLuS_2$:Tm and $KLuS_2$:Yb will be interesting materials for broad-band infrared laser construction.

Appendix A. Supplementary data

Supplementary data to this article can be found online at https://doi.org/10.1016/j.jlumin.2019.03.005.

Funding

This research has been supported by the Czech Science Foundation (project No. 18-11954S), by the Ministry of Education, Youth and Sports of Czech Republic (project No. LO1409), and by the Operational Programme Research, Development and Education financed by European Structural and Investment Funds and the Czech Ministry of Education, Youth and Sports (project SAFMAT – CZ.02.1.01/0.0/0.0/16_013/0001406).

References

[1] I.T. Sorokina, K.L. Vodopyanov (Eds.), Solid-State Mid-infrared Laser Sources, Springer-Verlag, Berlin, 2003Vol. 89 of Topics in Applied Physics.
[2] M. Ebrahim-Zadeh, I.T. Sorokina (Eds.), Mid-Infrared Coherent Sources and Applications, vol. 89, Springer Netherlands, Dordrecht, 2008, https://doi.org/10.1007/978-1-4020-6463-0.
[3] B. Henderson, G.F. Imbusch, Optical Spectroscopy of Inorganic Solids, Monographs on the Physics and Chemistry of Materials, Oxford University Press, Incorporated, 2006.
[4] Y.V. Orlovskii, T.T. Basiev, K.K. Pukhov, M.E. Doroshenko, V.V. Badikov, D.V. Badikov, O.K. Alimov, M.V. Polyachenkova, L.N. Dmitruk, V.V. Osiko, S.B. Mirov, Mid-IR transitions of trivalent neodymium in low phonon laser crystals, Opt. Mater. 29 (9) (2007) 1115–1128 https://doi.org/10.1016/j.optmat.2006.05.009.
[5] R.C. Powell, Physics of Solid-State Laser Materials, Atomic, Molecular and Optical Physics Series, Springer-Verlag, New York, 1998.
[6] J. Ganem, J. Crawford, P. Schmidt, N.W. Jenkins, S.R. Bowman, Thulium cross-relaxation in a low phonon energy crystalline host, Phys. Rev. B 66 (2002) 28012 https://doi.org/10.1103/PhysRevB.66.245101.
[7] J. Ganem, S.R. Bowman, Use of thulium-sensitized rare earth-doped low phonon energy crystalline hosts for IR sources, Nanoscale Res. Lett. 8 (1) (2013) 455 https://doi.org/10.1186/1556-276X-8-455.
[8] K. Nitsch, M. Dušek, M. Nikl, K. Polák, M. Rodová, Ternary alkali lead chlorides: crystal growth, crystal structure, absorption and emission properties, Prog. Cryst. Growth Char. Mater. 30 (1) (1995) 1–22 https://doi.org/10.1016/0960-8974(95)00012-V.
[9] K. Rademaker, Rare Earth-Doped Alkali-Lead-Halide Laser Crystals of Low-Phonon Energy, Cuvillier Verlag, Gottingen, 2005.
[10] L. Isaenko, A. Yelisseyev, A. Tkachuk, S. Ivanova, New monocrystals with low phonon energy for mid-IR lasers, in: M. Ebrahim-Zadeh, I.T. Sorokina (Eds.), Mid-Infrared Coherent Sources and Applications, Springer Netherlands, Dordrecht, 2008, pp. 3–65.
[11] M. Velázquez, A. Ferrier, J.-L. Doualan, R. Moncorgé, Rare-earth-doped low phonon energy halide crystals for mid-infrared laser sources, in: A.H. Al-Khursan (Ed.), Solid State Laser, IntechOpen, Rijeka, 2012 Ch. 4 https://doi.org/10.5772/38204.
[12] S. Payne, M. Nostrand, R. Page, P. Schunemann, L. Isaenko, Laser Demonstration of Rare-Earth Ions in Low Phonon Chloride and Sulfide Crystals, ASSL, OSA, 2000, p. MF4 https://doi.org/10.1364/ASSL.2000.MF4.
[13] S.R. Bowman, S.K. Searles, N.W. Jenkins, S.B. Qadri, E.F. Skelton, J. Ganem, New mid-IR laser based on an erbium activated low phonon energy crystal, Technical Digest. Summaries of Papers Presented at the Conference on Lasers and Electro-Optics. Postconference Technical Digest, 2001, pp. 557–558 (IEEE Cat. No. 01CH37170), https://doi.org/10.1109/CLEO.2001.948162.
[14] L. Isaenko, A. Yelisseyev, A. Tkachuk, S. Ivanova, S. Vatnik, A. Merkulov, S. Payne, R. Page, M. Nostrand, New laser crystals based on KPb_2Cl_5 for IR region, Mater. Sci. Eng., B 81 (1) (2001) 188–190 https://doi.org/10.1016/S0921-5107(00)00735-2.
[15] A.G. Okhrimchuk, L.N. Butvina, E.M. Dianov, N.V. Lichkova, V.N. Zagorodnev, A.V. Shestakov, New laser transition in a Pr^{3+}:$RbPb_2Cl_5$ crystal in the 2.3–2.5 -μm range, Quant. Electron. 36 (1) (2006) 41 https://doi.org/10.1070/QE2006v036n01ABEH013101.
[16] A.G. Okhrimchuk, L.N. Butvina, E.M. Dianov, I.A. Shestakova, N.V. Lichkova, V.N. Zagorodnev, A.V. Shestakov, Optical spectroscopy of the $RbPb_2Cl_5$:Dy^{3+} laser crystal and oscillation at 5.5 μm at room temperature, J. Opt. Soc. Am. B: Opt. Phys. 24 (10) (2007) 2690–2695 https://doi.org/10.1364/JOSAB.24.002690.
[17] L.D. DeLoach, R.H. Page, G.D. Wilke, S.A. Payne, W.F. Krupke, Transition metal-doped zinc chalcogenides: spectroscopy and laser demonstration of a new class of gain media, IEEE J. Quantum Electron. 32 (6) (1996) 885–895 https://doi.org/10.1109/3.502365.
[18] R. Page, K. Schaffers, L. DeLoach, G. Wilke, F. Patel, J. Tassano, S. Payne, W. Krupke, K.-T. Chen, A. Burger, Cr^{2+}-doped zinc chalcogenides as efficient, widely tunable mid-infrared lasers, IEEE J. Quantum Electron. 33 (4) (1997) 609–619 https://doi.org/10.1109/3.563390.
[19] T.J. Carrig, Transition-metal-doped chalcogenide lasers, J. Electron. Mater. 31 (7) (2002) 759–769 https://doi.org/10.1007/s11664-002-0233-1.
[20] V.A. Akimov, A.A. Voronov, V.I. Kozlovskii, Y.V. Korostelin, A.I. Landman, Y.P. Podmar'kov, M.P. Frolov, Efficient IR Fe:ZnSe laser continuously tunable in the spectral range from 3.77 to 4.40 μm, Quant. Electron. 34 (10) (2004) 912 https://doi.org/10.1070/QE2004v034n10ABEH002789.
[21] V. Fedorov, S. Mirov, A. Gallian, D. Badikov, M. Frolov, Y. Korostelin, V. Kozlovsky, A. Landman, Y. Podmar'kov, V. Akimov, A. Voronov, 3.77-5.05-μm tunable solid-state lasers based on Fe^{2+}-doped ZnSe crystals operating at low and room temperatures, IEEE J. Quantum Electron. 42 (9) (2006) 907–917 https://doi.org/10.1109/JQE.2006.880119.
[22] M.E. Doroshenko, H. Jelinkov, P. Koranda, J. Šulc, T.T. Basiev, V.V. Osiko, V.K. Komar, A.S. Gerasimenko, V.M. Puzikov, V.V. Badikov, D.V. Badikov, Tunable mid-infrared laser properties of Cr^{2+}:ZnMgSe and Fe^{2+}:ZnSe crystals, Laser Phys. Lett. 7 (1) (2010) 38–45 https://doi.org/10.1002/lapl.200910111.
[23] M.E. Doroshenko, V.V. Osiko, H. Jelínková, M. Jelínek, J. Šulc, D. Vyhlídal, N.O. Kovalenko, I.S. Terzin, Spectral and lasing characteristics of Fe:Cd_{1-x} Mn_xTe (x = 0.1-0.76) crystals in the temperature range 77 to 300 K, Opt. Mater. Express 8 (7) (2018) 1708–1722 https://doi.org/10.1364/OME.8.001708.
[24] T.T. Basiev, M.E. Doroshenko, V.V. Osiko, D.V. Badikov, Mid IR laser oscillations in new low phonon $PbGa_2$ S_4:Dy^{3+} crystal, in: C. Denman, I. Sorokina (Eds.), ASSL (TOPS), Vol. 98 of OSA Trends in Optics and Photonics, OSA, 2005, p. 75 https://doi.org/10.1364/ASSP.2005.75.
[25] M.E. Doroshenko, T.T. Basiev, V.V. Osiko, V.V. Badikov, D.V. Badikov, H. Jelínková, P. Koranda, J. Šulc, Oscillation properties of dysprosium-doped lead thiogallate crystal, Opt. Lett. 34 (5) (2009) 590–592 https://doi.org/10.1364/OL.34.000590.
[26] H. Jelínková, M.E. Doroshenko, M. Jelínek, J. Šulc, V.V. Osiko, V.V. Badikov, D.V. Badikov, Dysprosium-doped Pboped $PbGa_2S_4$ laser generating at 4.3 μm directly pumped by 1.7 μm laser diode, Opt. Lett. 38 (16) (2013) 3040–3043 https://doi.org/10.1364/OL.38.003040.
[27] L. Havlák, V. Jarý, M. Nikl, P. Boháček, J. Bárta, Preparation, luminescence and structural properties of RE-doped $RbLaS_2$ compounds, Acta Mater. 59 (16) (2011) 6219–6227 https://doi.org/10.1016/j.actamat.2011.06.019.
[28] V. Jarý, L. Havlák, J. Bárta, M. Nikl, Preparation, luminescence and structural properties of rare-earth-doped $RbLuS_2$ compounds, Phys. Stat. Solid. RRL 6 (2) (2012) 95–97 https://doi.org/10.1002/pssr.201105481.
[29] V. Jarý, L. Havlák, J. Bárta, E. Mihóková, M. Buryi, M. Nikl, $ALnS_2$:RE (A = K, Rb; Ln = La, Gd, Lu, Y): new optical materials family, J. Lumin. 170 (2016) 718–735 https://doi.org/10.1016/j.jlumin.2015.08.080.
[30] J. Fábry, L. Havlák, M. Dušek, P. Vaněk, J. Drahokoupil, K. Jurek, Structure determination of $KLaS_2$, $KPrS_2$, $KEuS_2$, $KGdS_2$, $KLuS_2$, KYS_2, $RbYS_2$, $NaLaS_2$ and crystal-chemical analysis of the group 1 and thallium(I) rare-earth sulfide series, Acta Crystallogr. B 70 (2) (2014) 360–371 https://doi.org/10.1107/S2052520613034574.
[31] V. Jarý, L. Havlák, J. Bárta, E. Mihóková, P. Průša, M. Nikl, Optical properties of Ce^{3+}-doped $KLuS_2$ phosphor, J. Lumin. 147 (2014) 196–201 https://doi.org/10.1016/j.jlumin.2013.11.013.

[32] V. Jarý, L. Havlák, J. Bárta, E. Mihóková, M. Nikl, Optical and structural properties of RE^{3+}-doped $KLnS_2$ compounds, IEEE Trans. Nucl. Sci. 61 (1) (2014) 385–389 https://doi.org/10.1109/TNS.2013.2277606.
[33] V. Jarý, L. Havlák, J. Bárta, M. Rejman, A. Bystřický, C. Dujardin, G. Ledoux, M. Nikl, Circadian light source based on $K_xNa_{1-x}LuS_2:Eu^{2+}$ phosphor, ECS J Solid State Sci. Technol. 7 (1) (2018) R3182–R3188 https://doi.org/10.1149/2.0231801jss.
[34] L. Havlák, J. Fábry, M. Henriques, M. Dušek, Structure determination of $KScS_2$, $RbScS_2$, and $KLnS_2$ (Ln = Nd, Sm, Tb, Dy, Ho, Er, Tm and Yb) and crystal-chemical discussion, Acta Crystallogr. C 71 (7) (2015) 623–630 https://doi.org/10.1107/S2053229615011833.
[35] J. Fábry, L. Havlák, M. Kučeráková, M. Dušek, Redetermination of $NaGdS_2$, $NaLuS_2$ and $NaYS_2$, Acta Crystallogr. C 70 (6) (2014) 533–535 https://doi.org/10.1107/S2053229614009607.
[36] V. Jarý, L. Havlák, J. Bárta, E. Mihóková, M. Nikl, Luminescence and structural properties of $RbGdS_2$ compounds doped by rare earth elements, Opt. Mater. 35 (6) (2013) 1226–1229 https://doi.org/10.1016/j.optmat.2013.01.028.
[37] S. Stoll, A. Schweiger, EasySpin, a comprehensive software package for spectral simulation and analysis in EPR, J. Magn. Reson. 178 (1) (2006) 42–55 https://doi.org/10.1016/j.jmr.2005.08.013.
[38] R.D. Shannon, Revised effective ionic radii and systematic studies of interatomic distances in halides and chalcogenides, Acta Crystallogr. A 32 (5) (1976) 751–767 https://doi.org/10.1107/S0567739476001551.
[39] A. Abragam, B. Bleaney, Electron Paramagnetic Resonance of Transition Ions, Clarendon Press, Oxford, 1970, pp. 560–568.
[40] J.E. Wertz, J.R. Bolton, Electron Spin Resonance: Elementary Theory and Practical Applications, McGraw-Hill, New York, 1980.
[41] V. Jarý, L. Havlák, J. Bárta, M. Buryi, E. Mihóková, M. Rejman, V. Laguta, M. Nikl, Optical, structural and paramagnetic properties of Eu-doped ternary sulfides $ALnS_2$ (A = Na, K, Rb; Ln = La, Gd, Lu, Y), Materials 8 (10) (2015) 6978–6998 https://doi.org/10.3390/ma8105348.
[42] F.A. Cotton, Chemical Applications of Group Theory, third ed., John Wiley and Sons, New-York, 1990.
[43] B.R. Judd, The magnetic and spectroscopic properties of certain rare-earth double nitrates, Proc. Roy. Soc. Lond. A 232 (1191) (1955) 458–474 https://doi.org/10.1098/rspa.1955.0231.
[44] P. Brüesch, C. Schüler, Raman and infrared spectra of crystals with α-$NaFeO_2$ structure, J. Phys. Chem. Solids 32 (5) (1971) 1025–1038 https://doi.org/10.1016/S0022-3697(71)80347-5.
[45] C.M. Dodson, R. Zia, Magnetic dipole and electric quadrupole transitions in the trivalent lanthanide series: calculated emission rates and oscillator strengths, Phys. Rev. B 86 (2012) 125102https://doi.org/10.1103/PhysRevB.86.125102.